Calculation of optical and K pre-edge absorption spectra for ferrous iron of distorted sites in oxide crystals

Vincent Vercamer,[1,2] Myrtille O. J. Y. Hunault,[1] Gérald Lelong,[1] Maurits W. Haverkort,[3] Georges Calas,[1] Yusuke Arai,[4] Hiroyuki Hijiya,[4] Lorenzo Paulatto,[1] Christian Brouder,[1] Marie-Anne Arrio,[1] and Amélie Juhin[1]

[1]*Sorbonne Universités, UPMC Univ Paris 06, CNRS, IRD, MNHN, Institut de Minéralogie, de Physique des Matériaux et de Cosmochimie, 4 place Jussieu, 75252 Paris cedex 05, France*

[2]*AGC France SAS, 100 rue Léon Gambetta, 59168 Boussois, France*

[3]*Max Planck Institute for Chemical Physics of Solids, Nöthnitzer Straße 40, 01187 Dresden, Germany*

[4]*Research Center, Asahi Glass Co. Ltd., 1150 Hazawa-cho, Kanagawa-ku, Yokohama 221-8755, Japan*

(Received 7 October 2016; published 7 December 2016)

Advanced semiempirical calculations have been performed to compute simultaneously optical absorption and K pre-edge x-ray absorption spectra of Fe^{2+} in four distinct site symmetries found in minerals. The four symmetries, i.e., a distorted octahedron, a distorted tetrahedron, a square planar site, and a trigonal bipyramidal site, are representative of the Fe^{2+} sites found in crystals and glasses. A particular attention has been paid to the definition of the p-d hybridization Hamiltonian which occurs for noncentrosymmetric symmetries in order to account for electric dipole transitions. For the different sites under study, an excellent agreement between calculations and experiments was found for both optical and x-ray absorption spectra, in particular in terms of relative intensities and energy positions of electronic transitions. To our knowledge, these are the first calculations of optical absorption spectra on Fe^{2+} placed in such diverse site symmetries, including centrosymmetric sites. The proposed theoretical model should help to interpret the features of both the optical absorption and the K pre-edge absorption spectra of 3d transition metal ions and to go beyond the usual fingerprint interpretation.

DOI: 10.1103/PhysRevB.94.245115

I. INTRODUCTION

Computing the absorption cross-section of electronic transitions is still a major challenge in the field of spectroscopy. In the words of Bersuker and Polinger: "the problem of the explanation of relative and absolute intensities of spectral lines stands out today as one of the most important in the whole field of spectroscopy" [1]. Optical absorption spectroscopy (OAS) and K pre-edge x-ray absorption spectroscopy (XAS) are complementary experimental techniques that enable to determine and compare the speciation of transition metal (TM) ions by probing their 3d shells. Local symmetry is a key parameter that governs electronic, magnetic, and optical properties in materials. One of the most striking example of how local symmetry affects optical properties is illustrated by Co^{2+} ions, which give an intense blue color in a tetrahedral site, and a pale pink color when placed in an octahedral site [2]. Generally speaking, the absorption intensity for T_d symmetry will be larger than those for O_h symmetry for all 3d elements in both OAS and K pre-edge XAS. This general feature is often used as a criterion to distinguish site geometries [3–9].

Since the very beginning of crystal-field theory, computation of absorption spectra has partially enabled to go beyond a simple "fingerprint" interpretation. Calculations are indeed useful to extract physical quantities from experimental data, such as coordination number, local symmetry and distortion, oxidation and spin states, bond covalency, and orbital mixing. They are even more needed when the site is distorted or when several absorbing species coexist in the sample [10].

The intensity of spectral transitions is a meaningful information to identify distorted sites or to distinguish coexisting absorbing species. State-of-the-art calculations of absorption spectra do not reproduce accurately the absolute intensities of transitions that depend on both the nature of the transition operator and the nature of the initial and final electronic and vibronic states. Optical absorption of TM ions mostly originates from d-d electronic transitions, while the K pre-edge XAS involves transitions from 1s to 3d states. Consequently, both XAS and OAS are well suited to probe and describe the electronic structure of 3d states although in the case of XAS, they are perturbed by the 1s core hole.

In the case of XAS, the K pre-edge intensity depends on the proportion of *on-site* 3d-4p hybridization, which results in an additional electric dipole (E1) contribution arising from $1s \rightarrow 4p$ transitions, with respect to the electric quadrupole contribution (E2) originating from $1s \rightarrow 3d$ transitions. Using ligand field multiplet (LFM) calculations including p-d hybridization, Arrio *et al.* [11] reproduced the variation of XAS K pre-edge spectra for both Fe^{2+} and Fe^{3+} ions in T_d and O_h symmetries in Fe-bearing minerals. The inclusion of 3d-4p mixing in these calculations of the pre-edge features is a key issue, but they are often tedious for symmetries lower than O_h and T_d. Recently, following the same multielectronic semiempirical approach, Hunault and coworkers succeeded in calculating the XAS Co K pre-edge spectra for a Co^{2+} ion in T_d, O_h, D_{3h}, and C_{4v} symmetries [12], opening the way to the calculations of absorption cross sections of low-symmetry sites.

For OAS, according to the Laporte selection rule, only electric quadrupole transitions (E2) are allowed by parity. However, the E2 contribution is too weak to account for the entire intensity of optical absorption transitions [13]. The observation of nonzero transitions therefore suggests that electric dipole (E1) transitions occur despite Laporte rule interdiction. It has been generally assumed that this electric dipole contribution arises from the relaxation of the parity rule via static or dynamic (vibrations) distortions [14,15]. By removing the inversion center from the point group symmetry

 ©2016 American Physical Society

of the absorbing site, a $3d$-$4p$ mixing on the metal ion is then enabled [16].

A limited number of papers are devoted to the calculation of optical absorption spectra in terms of position and intensity of optical transitions [13,14,17–19]. This is mainly related to the difficulty to describe accurately with a unique theoretical approach both *on-site* multielectronic interactions and the electronic structure outside the nearest ligand atoms. In the past decades, a lot of efforts have been devoted to reproduce optical absorption spectra using *ab initio* approaches. First-principles configuration-interaction calculations (DFT-CI) coupled to sophisticated methods of lattice relaxation lead to undeniable progress [20,21]. Nevertheless, the results are still relatively disparate: a good overall agreement between experiment and theory was found for Cr^{3+} in α-Al_2O_3 [17,20,21] and for Co^{3+} in $[Co(NH_3)_6]^{3+}$ [19], while some discrepancies are found for Cr^{3+} in $BeAl_2O_4$ [20] or for V^{2+} in α-Al_2O_3 [17,21]. Even if such a methodology can give satisfactory results for relatively simple systems, it is hardly tractable for complex structures showing a low degree of symmetry as illustrated by the local environment of TM ions found in many minerals or glasses.

Our approach does not consist in calculating the crystal-field parameters but in measuring them by analyzing OAS and XAS spectra. The methodology proposed here is then based on the use of LFM approach including p-d hybridization in order to calculate both optical and x-ray absorption spectroscopies under the same theoretical frame. By calculating both spectroscopies simultaneously, parameters are limited in number, better constrained, and consecutively, more significant.

To our knowledge, no such optical absorption calculations have been done for Fe^{2+} compounds, and more specifically for iron-bearing silicates. In particular, the broad and asymmetrical shape of the Fe^{2+} band observed in the UV-visible-NIR absorption spectra of soda-lime silicate glasses remains a challenging question, for which only empirical methods based on fingerprint analysis are applied [22]. At this point, it is then essential to use a numerical approach allowing to interpret finely the origin of the absorption features of regular and distorted Fe^{2+} sites found in iron-bearing minerals.

In the present paper, we perform LFM calculations including metal *on-site* $3d$-$4p$ hybridization to compute jointly the absorption cross-section of optical and XAS K pre-edge spectra of iron in various site symmetries. This provides a deeper understanding of the origin of the absorption features of regular and distorted Fe^{2+} sites found in iron-bearing minerals. A special attention was paid to the definition of hybridization Hamiltonian for low symmetries in order to account for tetragonal or trigonal site distortions. These calculations enable us to compare the effect of local symmetry on transition intensities and to quantitatively assess $3d$-$4p$ hybridization for iron ions in various environments.

II. EXPERIMENTS

A. Samples

This work is focused on a benchmark set of four crystalline natural samples containing high-spin Fe^{2+} ions in various symmetries. Siderite ($FeCO_3$) is a yellow-brown carbonate containing $^{[6]}Fe^{2+}$ in a slightly distorted octahedral site sharing corners with other Fe-bearing octahedra [23,24]. The local geometry of Fe^{2+} is C_{3i} [25].

The staurolite ($Fe_4Al_{18}Si_8O_{46}(OH)_2$) sample is a dark orthosilicate mineral from Brittany, France. Iron is present as $^{[4]}Fe^{2+}$ in a distorted tetrahedron with a point group symmetry close to C_{2v} [26].

The gillespite ($BaFeSi_4O_{10}$) sample is a pink phyllosilicate mineral from Incline, California. Iron is present as $^{[4]}Fe^{2+}$ in an almost perfect square-planar site with a local geometry close to D_{4h} or C_{4v} [27].

The grandidierite [$(Mg,Fe)Al_3(BO_4)(SiO_4)O$] sample is a blue-green orthosilicate mineral from Ampamatoa, Madagascar, with 5.0 wt% FeO and an exceptional redox close to 99%, i.e., almost all Fe ions are found as Fe^{2+} in substitution of Mg^{2+}. Grandidierite is one of the rare minerals with a fivefold coordinated Fe^{2+}. The local geometry is a distorted triangular bipyramidal site represented by the point group C_s [28].

B. XAS measurements

XAS spectra were collected at the Fe K edge (7112 eV) at room temperature on the ID26 beamline of the ESRF (Grenoble, France). The incident beam was monochromatized using a Si(311) double crystal. XANES spectra were recorded from 7000 to 7500 eV in fluorescence mode using powder samples diluted into cellulose and a 90° angle between the incident and scattered beam. Data in the pre-edge (7110–7117 eV) and edge (7117–7180 eV) regions were recorded using a 0.05 eV energy step. Outside this range, a 1 eV step was used. 60 pre-edge spectra were collected and averaged for each sample. Spectra were normalized to an absorption step of 1 using ATHENA software [29] and then corrected from self-absorption. The pre-edge features presented in this paper are given after subtracting the tail of the main edge using an arctangent function.

C. Optical absorption measurements

Diffuse reflectance measurements were performed using a PerkinElmer Lambda 1050 spectrometer and a Praying Mantis™ accessory (Harrick Scientific Products Inc.), a highly efficient diffuse reflectance collection system that minimizes the detection of the specular component. Samples were prepared as finely ground powders deposited on aluminum sample holders. Optical spectra were recorded in the range 4000–33000 cm^{-1}. Assuming particle size of the order of the wavelength and low absorption, we apply the Kubelka-Munk approximation, which defines the remission function $F(R_\infty)$ as:

$$F(R_\infty) = \frac{K}{S} = \frac{(1-R_\infty)^2}{2R_\infty}, \quad (1)$$

where the limiting reflectance is $R_\infty = 10^{-A}$ with A the absorbance, K is the absorption coefficient and S the scattering coefficient [30]. Diffuse reflectance measurements do not provide a direct estimation of the molar extinction coefficient (characteristic of an absorbent species) but rather an estimate of it. It can be used to compare different compounds assuming the scattering coefficients are identical for all samples. For

grandidierite, the optical spectra are taken from the literature [31].

III. THEORY

A. Ligand field multiplet (LFM) framework

OAS and XAS spectra were calculated using LFM theory. A method that includes all local interactions and allows for electronic entanglement. The empirical crystal-field potential is chosen in order to reproduce the low energy eigenorbitals and as such not related to realistic electrostatic fields in the crystal. For core level spectroscopy the method was initially devised by Thole *et al.* [32] in the framework established by Cowan [33] and Butler [34]. In this approach, one considers an isolated Fe^{2+} ion embedded in a crystal-field potential with an additional term that mixes $3d$ and $4p$ orbitals describing the *on-site* $3d$-$4p$ hybridization. It takes into account all the $3d$-$3d$ and $1s$-$3d$ electronic Coulomb interactions, as well as the spin-orbit coupling ζ on every open shell of the absorbing atom. Each of these many-body states is described by a linear combination of Slater determinants [33]. More details on the method can be found in other references [35].

1. Description of the Hamiltonian

The Hamiltonian describing a given multielectronic state of the absorbing ion is written as:

$$H = H_{\text{kin}} + H_{e/N} + H_{e/e} + H_{\text{SO}} + H_{\text{CF}} + H_{\text{Hyb}}, \qquad (2)$$

where H_{kin} is the kinetic energy of the electrons, $H_{e/N}$ the electrostatic interaction of the electrons with the nuclei, $H_{e/e}$ the electron-electron interaction, and H_{SO} is the spin-orbit coupling. The influence of the local symmetry is described using the crystal-field Hamiltonian H_{CF}, which takes into account the local environment around the absorbing atom. The hybridization Hamiltonian H_{Hyb} mixes appropriate d and p orbitals and describes the *on-site* $3d$-$4p$ mixing. (See below.) Both H_{CF} and H_{Hyb} depend on parameters regarding the site geometry, interaction with neighboring ligands and the point group symmetry [11,36]. Note that charge transfer effects (i.e., *off-site* transitions from the $3d$ orbitals of the transition metal to the $2p$ orbitals of the ligands) are not taken into account in this model but the ionocovalency of the Fe-O bond is taken into account through the nephelauxetic ratio β that is applied to reduce Slater integrals from their atomic values.

For OAS and XAS, the initial state configuration of the system is built from the combination of two electronic configurations, $1s^2 3d^n 4p^0$ and $1s^2 3d^{n-1} 4p^1$ (with $n = 6$ for Fe^{2+}), as illustrated in Fig. 1. For OAS, the final state is described by the same configuration interaction, while the final state configuration of XAS is built with a $1s$ core hole from the combination of the two electronic configurations $1s^1 3d^{n+1} 4p^0$ and $1s^1 3d^n 4p^1$.

Both crystal-field and hybridization Hamiltonians are expanded on renormalized spherical harmonics:

$$H_{\text{CF/Hyb}} = \sum_{k=0}^{\infty} \sum_{m=-k}^{k} A_{k,m} C_{k,m}(\theta,\phi), \qquad (3)$$

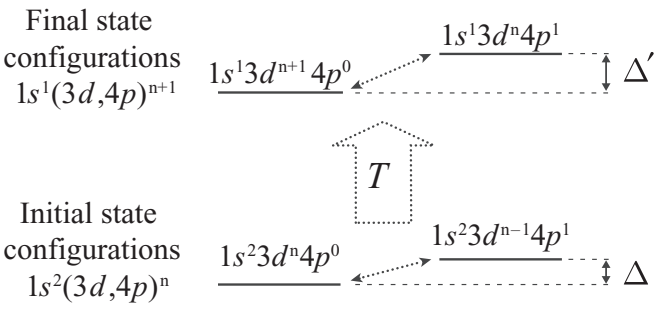

FIG. 1. Configuration interaction used to describe the *on-site* $4p$–$3d$ mixing in the XAS initial and final state configurations. T is the transition operator defined in Eq. (3).

where the renormalized spherical harmonics are defined by [33]

$$C_{k,m}(\theta,\phi) = \sqrt{\frac{4\pi}{2k+1}} Y_{k,m}(\theta,\phi) \qquad (4)$$

and the $A_{k,m}$ are expressed in Appendix A. For $3d$ transition metals, the crystal-field Hamiltonian writes [34,37–39]

$$H_{\text{CF}} = \sum_{\substack{k=0,\\ k \text{ even}}}^{4} \sum_{m=-k}^{k} A_{k,m} C_{k,m}(\theta,\phi). \qquad (5)$$

The site symmetry of the absorbing ion determines which $A_{k,m}$ are nonzero. The nonzero $A_{k,m}$ can be related either to the parameters often used in OAS such as Dq, Ds, Dt, $D\sigma$, $D\tau$ or to the energies of the monoelectronic $3d$ orbitals (as obtained from DFT calculations). These relations are given in Appendix B [37]. The list of parameters to be considered for each symmetry is summarized in Table I.

In the case of a $3d$ transition metal in a noncentrosymmetric site, the hybridization Hamiltonian mixes the $3d$ ($\ell = 2$) with the $4p$ ($\ell = 1$) states. It is given by:

$$H_{\text{Hyb}} = \sum_{\substack{k=1,\\ k \text{ odd}}}^{3} \sum_{m=-k}^{k} A_{k,m} C_{k,m}(\theta,\phi). \qquad (6)$$

The mixing rules between the d and p orbital is imposed by the symmetry of H_{Hyb}. The hybridization Hamiltonian is

TABLE I. List of crystal-field and hybridization parameters for each symmetry, and decomposition of E1 and E2 transition operators into irreducible representations. We use the definitions from König and Kremer [37].

Site	Hamiltonians		Transition operator	
symmetry	H_{CF} [37]	H_{Hyb}	E1	E2
O_h	$10Dq$	–	–	$E_g \oplus T_{2g}$
T_d	$10Dq$	$V_{pd}^{t_2}$	T_2	$E \oplus T_2$
C_{4v}	Dq, Ds, Dt	$V_{pd}^{a_1}$, V_{pd}^{e}	$A_1 \oplus E$	$A_1 \oplus B_1 \oplus B_2 \oplus E$
C_{3v}	Dq, $D\sigma$, $D\tau$	$V_{pd}^{a_1}$, $V_{pd}^{e(e_g)}$, $V_{pd}^{e(t_{2g})}$	$A_1 \oplus E$	$A_1 \oplus 2E$

decomposed in a sum of terms using point group theory:

$$H_{\mathrm{Hyb}}^{G} = \sum_{i} H_{\mathrm{Hyb}}^{\Gamma_i}, \tag{7}$$

where G is the group symmetry of H_{Hyb} and Γ_i is an irreducible representation of G that allows mixing between d and p orbitals. Each $H_{\mathrm{Hyb}}^{\Gamma_i}$ Hamiltonian is parametrized by the mixing parameter $V_{pd}^{\Gamma_i}$. For instance in T_d point group symmetry, the hybridization Hamiltonian couples p_x, p_y, and p_z orbitals of t_2 symmetry with the d_{xy}, d_{xz} and d_{yz} orbitals that also have t_2 symmetry. The hybridization Hamiltonian itself has the full T_d symmetry (it is an a_1 irreducible representation). The hybridization parameter is labeled $V_{pd}^{t_2}$. For each symmetry considered, the composition of H_{Hyb} and the relations between $V_{pd}^{\Gamma_i}$ and $A_{k,m}$ parameters are given in Appendix B. The list of hybridization parameters for each symmetry is summarized in Table I.

2. *Calculation of absorption cross-sections*

For XAS, in the case of noncentrosymmetric sites, E1 ($1s \rightarrow 4p$) and E2 ($1s \rightarrow 3d$) transitions contribute to the absorption cross-section. For linear polarization of the incident beam and a nonmagnetic sample (no net magnetic moment on the absorbing ion), there is no interference between the E1 and E2 terms [40]. Therefore the absolute absorption cross-section is directly calculated (and expressed in Å^2) as the sum of the E1 absorption cross-section σ_{dip} and the E2 absorption cross-section σ_{quad}:

$$\sigma(\hbar\omega) = \sigma_{\mathrm{dip}}(\hbar\omega) + \sigma_{\mathrm{quad}}(\hbar\omega) \tag{8}$$

with

$$\sigma_{\mathrm{dip}}(\hbar\omega) = 4\pi^2 \hbar\omega\alpha\, a_0^2 \left(P_{1s,4p}^{(1)}\right)^2 \mathcal{S}_{\mathrm{iso}}^{D} \tag{9}$$

and

$$\sigma_{\mathrm{quad}}(\hbar\omega) = 4\pi^2 \hbar\omega\alpha \left(\frac{a_0^2 \hbar\omega}{2\hbar c}\right)^2 \left(P_{1s,3d}^{(2)}\right)^2 \mathcal{S}_{\mathrm{iso}}^{Q}, \tag{10}$$

where a_0 is the Bohr radius, α is the fine structure constant, $\hbar$ is the Planck constant in eV.s, c is the speed of light, $P_{\ell,\ell'}^{(k)} = \langle n\ell||r^{(k)}||n\ell'\rangle$ is the monoelectronic radial matrix element (unitless), $k = 1$ for dipole operator and $k = 2$ for quadrupole operator [11,33].

The isotropic spectra $\mathcal{S}_{\mathrm{iso}}^{D}$ and $\mathcal{S}_{\mathrm{iso}}^{Q}$ are calculated using Green functions:

$$\mathcal{S} = \frac{-\mathrm{Im}(G(\omega))}{\pi}, \tag{11}$$

with

$$G(\omega) = \langle \psi_i | T^{\dagger} \frac{1}{\omega - H + i\Gamma/2} T | \psi_i \rangle, \tag{12}$$

where ψ_i is a many-particle wave function from the initial state, T is the transition operator, ω is the energy, H is the Hamiltonian of the system in the final state, and Γ is the $1s$ core-hole lifetime. For E1 and E2 transitions, T is defined as:

$$T = \boldsymbol{\varepsilon}.r + \frac{i}{2}(\boldsymbol{\varepsilon}.r)(k.r). \tag{13}$$

For OAS, optical transitions are exclusively electric dipole (magnetic dipole or electric quadrupole transitions are negligible) [13].

B. Computational details

Calculations were performed using the code Quanty [39] that uses second quantization and Lanczos recursion method to calculate Green functions [41], thus avoiding the explicit calculation of final states. The number of $3d$ and $4p$ electrons in the ground state built from the configuration interaction, respectively $\langle N_{3d}\rangle$ and $\langle N_{4p}\rangle$, were determined using the number operator that counts the electrons in the $n\ell$ shell: $N_{n\ell} = \sum_{m=-\ell}^{\ell} a_{n\ell m}^{\dagger} a_{n\ell m}$.

Regarding the ionocovalent behavior of the chemical bond in minerals, we applied for all minerals the same reduction factor β in both initial and final states. β multiplies the Slater integrals calculated for an isolated ion and was taken close to 60%. The spin-orbit coupling was considered at 100% of its free ion value ($\zeta_{3d} = 0.052$ eV) in agreement with previous studies [3,11].

For OAS, the initial and final states are described by the same sets of crystal-field and hybridization parameters. For XAS, the excited state is possibly described using a set of crystal-field parameters different from the initial state (see Table II).

The p-d hybridization Hamiltonian H_{hyb} depends on Δ, the difference between the average energies of the two electron configurations in the initial states ($1s^2 3d^6 4p^0$ and $1s^2 3d^5 4p^1$), and on Δ' which is the energy difference between the configurations $1s^1 3d^7 4p^0$ and $1s^1 3d^6 4p^1$, as illustrated in Fig. 1. For Fe^{2+}, the free ion values obtained from Hartree-Fock calculations are $\Delta = 12.6$ eV and $\Delta' = 13.8$ eV. The same values were used for the ion surrounded by ligands.

The XAS absolute intensities were calculated at $T = 300$ K and the population of the initial states is given by the Boltzmann law. The XAS K pre-edge spectra were convoluted by a Lorentzian function (full width at half maximum (FWHM): $\Gamma = 1.12$ eV) and a Gaussian function (FWHM: 0.35 to 0.42 eV), which respectively account for the $1s$ core-hole lifetime of Fe and for the instrumental resolution and sample imperfections. The monoelectronic radial matrix elements were calculated using a Hartree-Fock approach: for Fe^{2+}, $P_{1s,4p}^{(1)} = 0.00333$, and $P_{1s,3d}^{(2)} = 0.00090$. Finally, the transitions were normalized by the edge jump at the Fe K edge, calculated for a Fe atom as 3.3×10^{-4} Å^2 [42]. Hence the calculated XAS spectra can be directly compared to the experimental data normalized to the edge.

For optical absorption spectrum, $P_{1s,4p}^{(1)}$ is replaced by $P_{3d,4p}^{(1)} = 1.02866$. Optical absorption spectra were calculated with a small Lorentzian broadening ($\Gamma = 0.01$ eV), and cross-sections were further convoluted with a Gaussian function (FWHM: 0.15 to 0.30 eV). Note however that OAS theoretical cross-sections were rescaled to the experiment using the maximum of intensity in the UV-visible-NIR range.

IV. RESULTS

In the following, for clarity, we use the Schönflies notation without spin-orbit coupling to label multielectronic states.

TABLE II. Symmetry, coordination number (CN), and crystal-field (CF) and hybridization (Hyb) parameters used for calculating the optical and x-ray absorption spectra of the four compounds under study. The electron configuration $1s^2(3d,4p)^6$ is used for the initial and final states of OAS and for the XAS initial states. The excited electron configuration $1s^1(3d,4p)^7$ (with core-hole) is used only for the XAS final states.

Sample	Symmetry (CN)	$1s^2(3d,4p)^6$ CF (eV)	$1s^2(3d,4p)^6$ Hyb (eV)	$1s^1(3d,4p)^7$ CF (eV)	$1s^1(3d,4p)^7$ Hyb (eV)	Ground-state symmetry
Siderite	C_{3v} (6)	$Dq = 0.113$	$V_{pd}^{a_1(t_{2g})} = 0.33$	$Dq = 0.113$	$V_{pd}^{a_1} = 0.33$	${}^5E(T_{2g})$
		$D\sigma = -0.003$	$V_{pd}^{e(e_g)} = 0.06$	$D\sigma = -0.003$	$V_{pd}^{e(e_g)} = 0.06$	
		$D\tau = -0.020$	$V_{pd}^{e(t_{2g})} = 0.35$	$D\tau = -0.020$	$V_{pd}^{e(t_{2g})} = 0.35$	
Staurolite	T_d (4)	$Dq = -0.140$	$V_{pd}^{t_2} = 3.27$	$Dq = -0.140$	$V_{pd}^{t_2} = 3.27$	${}^5E(E_g)$
Gillespite	C_{4v} (4)	$Dq = 0.148$	$V_{pd}^{a_1} = 0.25$	$Dq = 0.161$	$V_{pd}^{a_1} = 0.25$	${}^5A_1(E_g)$
		$Ds = 0.470$	$V_{pd}^{e} = 0.10$	$Ds = 0.236$	$V_{pd}^{e} = 0.10$	
		$Dt = 0.120$		$Dt = 0.149$		
Grandidierite (site A)	C_{3v} (5)	$Dq = -0.050$	$V_{pd}^{a_1(t_{2g})} = 0.90$	$Dq = -0.045$	$V_{pd}^{a_1} = 0.90$	${}^5E(E_g)$
		$D\sigma = -0.010$	$V_{pd}^{e(e_g)} = 0.20$	$D\sigma = -0.009$	$V_{pd}^{e(e_g)} = 0.20$	
		$D\tau = -0.090$	$V_{pd}^{e(t_{2g})} = 1.65$	$D\tau = -0.081$	$V_{pd}^{e(t_{2g})} = 1.65$	
Grandidierite (site B)	C_{3v} (5)	$Dq = -0.045$	$V_{pd}^{a_1(t_{2g})} = 0.90$	$Dq = -0.041$	$V_{pd}^{a_1} = 0.90$	${}^5E(E_g)$
		$D\sigma = -0.050$	$V_{pd}^{e(e_g)} = 0.20$	$D\sigma = -0.045$	$V_{pd}^{e(e_g)} = 0.20$	
		$D\tau = -0.120$	$V_{pd}^{e(t_{2g})} = 1.65$	$D\tau = -0.108$	$V_{pd}^{e(t_{2g})} = 1.65$	

A. $^{[6]}Fe^{2+}$ in octahedral geometry

The experimental optical absorption spectrum of Fe^{2+} in siderite ($FeCO_3$) is presented in Fig. 2(a). We observe that the main optical transition centered around 9000 cm^{-1}, is split into two contributions at 8000 and 9600 cm^{-1}. In the approximation of an O_h site symmetry, this band is assigned to the spin-allowed transition ${}^5T_{2g} \rightarrow {}^5E_g$ [43]. For $[Fe(H_2O)_6]^{2+}$, the splitting of the ${}^5T_{2g} \rightarrow {}^5E_g$ transition has been explained by a dynamic Jahn-Teller effect [44]. Here, for $FeCO_3$, the Fe site shows a trigonal distortion and the real point group symmetry is C_{3i} (also named S_6) [25]. In octahedral C_{3i} symmetry, the ground state, that comes from the ${}^5T_{2g}$ level of O_h, splits into ${}^5E_g$ and ${}^5A_g$ terms as shown in Fig. 3. The ground state of Fe^{2+} is then the ${}^5E_g$ level [named ${}^5E_g(T_{2g})$]. The ${}^5E_g$ term in O_h is not split by trigonal distortion and is named ${}^5E_g(E_g)$ in C_{3i}. The transition from the ground state ${}^5E_g(T_{2g})$ to the ${}^5A_g$ level occurs in the infrared around 1400 cm^{-1}. We further observe weak absorption bands around 15000 cm^{-1}, which can be assigned to spin-forbidden transitions [44].

In agreement with previous studies on siderite [25,45,46], the C_{3v} point group was used in calculations instead of C_{3i}. Like O_h and D_{3d}, that are often used to approximate the Fe^{2+} site in siderite, C_{3i} is a centrosymmetric point group that does not allow p-d mixing, and thus gives zero values when E1 transitions are calculated. The approximation of C_{3i} by C_{3v} (that are both subgroups of O_h and D_{3d}) removes the inversion center and thus allows p-d mixing. This approximation has no influence on the transition energies or on the degeneracy of the energy levels since the crystal-field Hamiltonian is identical for both groups. The hybridization Hamiltonian in C_{3v} symmetry (detailed in Appendix B 2) is quantified using three parameters, $V_{pd}^{e(e_g)}$, $V_{pd}^{e(t_{2g})}$ and $V_{pd}^{a_1(t_{2g})}$, whose values are given in Table II.

With the crystal-field and hybridization Hamiltonians in C_{3v} point group, we calculated two optical absorption transitions with $\beta = 0.59$ and an optical Gaussian broadening with FWHM of 0.23 eV (1855 cm^{-1}). The two bands were named using C_{3v} terms (see Fig. 3) and were attributed to ${}^5E(T_{2g}) \rightarrow {}^5E(E_g)$ for the one at 9085 cm^{-1} and ${}^5E(T_{2g}) \rightarrow {}^5A_1$ for the other in the far infrared around 1400 cm^{-1} [see Fig. 2(a)]. The parameters listed in Table II show that Dq is the most significant parameter, while $D\sigma$ and $D\tau$ remain small. Although this confirms that Fe^{2+} in siderite remains in an O_h site with a preponderant cubic character, this calculation demonstrates the need to include the trigonal distortion in order to explain the infrared transition around 1400 cm^{-1}, which would not occur otherwise. With the weak hybridization potential used to compute nonzero transition intensities, the energies of the electronic states remain almost unchanged from the case without hybridization (the energy shift is lower than 1%, e.g., 75 cm^{-1} for the main transition around 9000 cm^{-1}). The inclusion of spin-orbit coupling in the calculation further enables to reproduce the weak spin-forbidden transitions around 15000 cm^{-1}.

The splitting of the ${}^5E$ band at 9000 cm^{-1} cannot be explained by C_{3i} site symmetry and was not reproduced in our calculations. Several explanations can be brought forward: (1) a lower symmetry of the real Fe^{2+} site, that can be related to dynamic Jahn-Teller effect, which can split the E level into two levels to minimize electronic repulsion; and (2) the presence of two slightly different sites in the mineral under study.

However, to our knowledge, no evidence of such partition has been reported in the literature. In the Tanabe-Sugano diagram of d^6 ion in O_h symmetry, the ${}^5E_g(D)$ level crosses the ${}^3T_{1g}(H)$ and ${}^1A_{1g}(I)$ levels around the Dq value used for the present calculations. Such a small energy difference between spin-allowed and spin-forbidden transitions could lead to increase the intensity of spin-forbidden transitions by spin-spin or vibration coupling that are not taken into account in this model.

The XAS K pre-edge shown in Fig. 2(b) presents three main features spread over 2 eV and a maximum intensity that is 2% of the edge jump and a small total pre-edge area

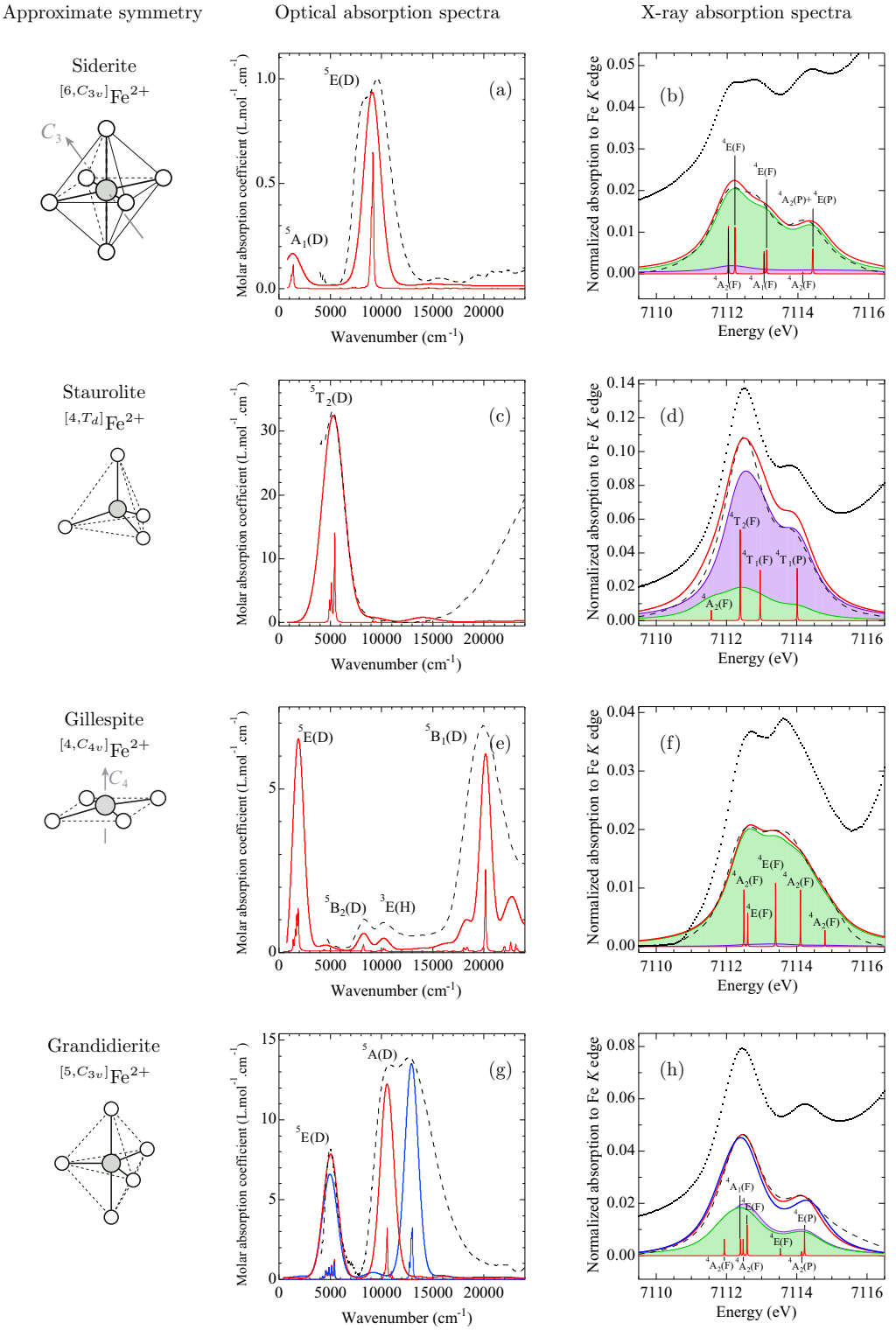

FIG. 2. Optical (left) and x-ray (right) spectra of siderite [(a) and (b)], staurolite [(c) and (d)], gillespite [(e) and (f)], and grandidierite [(g) and (h)]. The experimental and calculated OAS spectra are in black dashed line (– –) and in bold red line (——), respectively. The assignment of the transitions from the ground state is given for each symmetry. The experimental XAS data are in black lines: not corrected (· · ·) and corrected (– –) from the main edge tail. The calculated XAS K pre-edge spectra are in bold red line (——). Purple and green curves represent the respective contributions of the electric dipole and quadrupole transitions. The assignment of transitions is given using the $3d^7$ approximation. For grandidierite, simulated spectra for site A are in red, and spectra for site B are in blue, E1 and E2 XAS features are given for site A only (because they are very similar for site B).

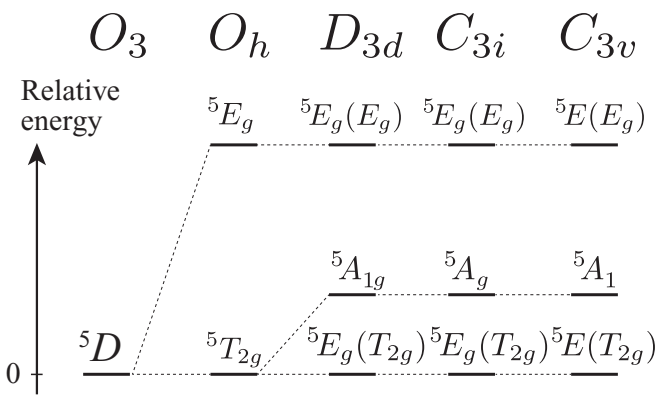

FIG. 3. Lifting of degeneracy of the ^5D spectroscopic term (free Fe^{2+} ion) caused by trigonal distortion in the case of siderite.

$A_{exp} = 5.9 \times 10^{-2}$ eV. For the XAS ground state, crystal-field and hybridization parameters were identical to those used for the OAS calculation. The parameters used for the excited state (with a $1s$ core hole) were taken equal to the ground-state parameters (Table II), which enabled us to reproduce accurately the experimental XAS spectra as shown in Fig. 2(b). The calculated spectrum was broaden with a Gaussian of FWHM = 0.4 eV.

Using weak V_{pd} parameters for C_{3v} hybridization the total pre-edge area is $A_{sum} = 6.4 \times 10^{-2}$ eV, which is close to the experimental value. Regarding the dipole and quadrupole contributions ($A_{dip} = 3.5 \times 10^{-3}$ eV and $A_{quad} = 6.1 \times 10^{-2}$ eV), the E1 part of the spectrum remains negligible (5.4% of the total area), which confirms that the intensity only comes from the E2 contribution. The calculated spectrum is similar to the one calculated for Fe^{2+} in siderite by Arrio *et al.* [11] using O_h symmetry without p-d mixing, which further confirms that the intensity in mainly due to E2 transitions.

For clarity, the attribution of the XAS transitions is done in the approximation of a $3d^{n+1}$ ion without core hole [47]. Three groups of peaks are observed at 7112 eV [$^4A_2(F) \oplus ^4E(F)$], 7113 eV [$^4A_1(F) \oplus ^4E(F)$], and 7114.5 eV [$^4A_2(P) \oplus ^4E(P)$], respectively. These terms are consistent with the attribution proposed by Westre *et al.* in O_h point group [3]: $^4T_{1g}(F)$, $^4T_{2g}(F)$ and $^4T_{1g}(P)$, which confirms that the Fe site is rather regular.

By studying ferrous iron in siderite, it has been shown that OAS is more sensitive than XAS to slight distortion of the local environment of C_{3v} symmetry. By crossing the results from these two spectroscopies using the same sets of parameters for calculations we demonstrate that Fe^{2+} site in siderite remains close to regular octahedral geometry (similar crystal-field values and energy levels). In addition, we prove that the O_h approximation is sufficient for XAS K pre-edge calculation regarding the experimental energy resolution.

B. $^{[4]}Fe^{2+}$ in tetrahedral geometry

In the case of staurolite, Fe^{2+} ions occupy a nonregular tetrahedral site with C_{2v} point group [26]. However, the T_d point group is often considered as an approximation for the interpretation of the Fe^{2+} local environment in staurolite [8,11,44,48].

The experimental OAS spectrum [Fig. 2(c)] shows one main transition, located around 5000 cm^{-1} which is assigned to the $^5E \rightarrow ^5T_2$ transition in T_d symmetry. Polarization-dependent OAS spectra from Rossman and Taran [31] show that the band around 5000 cm^{-1} is experimentally split into three bands located at 3800, 4600, and 5500 cm^{-1}. This lifting of degeneracy is assigned to the splitting of the $^5T_2$ level due to the site distortion. Nevertheless, for this case, the energy difference between the electronic levels is small compared to other minerals with tetrahedral Fe site such as pellyite [$Ba_2Ca(Fe,Mg)_2Si_6O_{17}$], which allows us to consider the T_d point group in a first approximation for the calculations [31].

In order to calculate the OAS of Fe in siderite, we used T_d symmetry for both the crystal-field and the hybridization Hamiltonians. Parameters used for the calculation are listed in Table II, β was taken equal to 0.62 and optical spectra were broaden by a Gaussian of FWHM = 0.3 eV (2420 cm^{-1}). Figure 2(c) compares theoretical and experimental spectra in which the main transition occurs around 5000 cm^{-1}. By applying 100% of the spin-orbit coupling, the $^5E \rightarrow ^5T_2$ transition is split into two components separated by 500 cm^{-1}, which is not enough to reproduce the experimental splitting. In order to take into account the distortion of the Fe^{2+} tetrahedron, a lower point group symmetry such as C_{2v} should be considered, with the drawback of increasing the number of parameters in the calculation.

The experimental XAS pre-edge spectrum [Fig. 2(d)] is 4.5 times more intense than for sixfold coordinated Fe (see previous case) and shows only two main features separated by 1.4 eV, which accounts for a smaller crystal-field splitting than in pseudo-octahedral symmetry.

The calculated Fe K pre-edge spectrum broadened with a Gaussian of FWHM = 0.35 eV in addition to the core-hole lifetime broadening, reveals four peaks at 7111.6, 7112.4, 7113, and 7114 eV assigned using the $3d^{n+1}$ approximation to the transitions $^5E(D) \rightarrow ^4A_2(F)$, $^5E(D) \rightarrow ^4T_2(F)$, $^5E(D) \rightarrow ^4T_1(F)$, and $^5E(D) \rightarrow ^4T_1(P)$, respectively [47].

The total area of the calculated pre-edge is $A_{sum} = 29.4 \times 10^{-2}$ eV, which is 26% higher than the total experimental area $A_{exp} = 23.3 \times 10^{-2}$ eV because the second peak around 7114 eV has a stronger intensity in the calculation than in the measurement. The area of the electric dipole is $A_{dip} = 23.6 \times 10^{-2}$, which is four times higher than the area of electric quadrupole contribution $A_{quad} = 5.8 \times 10^{-2}$ eV. Therefore despite the small number of $4p$ electrons ($\langle N_{4p} \rangle = 0.117$), 80% of the pre-edge area is due to E1 transitions, highlighting the strong effect of the $3d$-$4p$ mixing on electronic transitions in T_d symmetry.

C. $^{[4]}Fe^{2+}$ in square planar geometry

We now consider the case of gillespite ($BaFeSi_4O_{10}$), a rare silicate mineral in which ferrous iron is fourfold coordinated in a site close to a centrosymmetric square planar geometry. Regarding crystallographic data, the Fe^{2+} ion is slightly off the plane (by 0.027 Å) formed by the four oxygen ligands ($d_{Fe\text{-}O}$ = 1.984 Å) [27]. This distortion leads to the noncentrosymmetric C_{4v} point group that has been used for our calculations and the

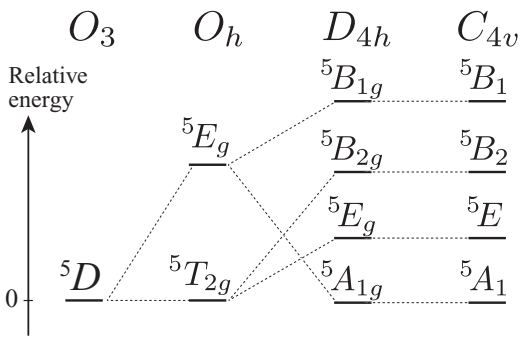

FIG. 4. Lifting of degeneracy of the ^5D spectroscopic term (free Fe^{2+} ion) caused by tetragonal distortion in the case of gillespite.

description of the transitions. The tetragonal distortion induces the splitting of the ^5D spectroscopic term as shown in Fig. 4. For sites with a point group lower than cubic, the number of crystal-field parameters necessary to describe the energy of the different levels increases, and here we used the crystal-field parameters Dq, Ds, and Dt [37,43,49]. In the case of the square-planar geometry, described in C_{4v}, the ground state of Fe^{2+} is $^5A_1$.

The experimental optical spectrum of gillespite [Fig. 2(e)] presents two features at 8250 and 20000 cm^{-1}, attributed to $^5A_1 \rightarrow {}^5B_2$ and $^5A_1 \rightarrow {}^5B_1$ transitions, respectively [50,51]. Another feature is present at 1150 cm^{-1} and is attributed to the first possible spin-allowed transition $^5A_1 \rightarrow {}^5E$.

C_{4v} symmetry was used for both the crystal-field and the hybridization Hamiltonians, the Slater integrals were reduced by $\beta = 0.64$ and the optical transitions broadened by a Gaussian function with a FWHM of 0.15 eV (1210 cm^{-1}); the corresponding parameters are listed in Table II. Since the site point group is almost centrosymmetric, we set the mixing parameters to small values ($V_{pd}^{a_1} = 0.25$ eV and $V_{pd}^{e} = 0.10$ eV), allowing the calculation of optical transitions. The energy position and relative intensities of the spin-allowed transitions are well reproduced with the crystal-field parameters given in Table II. Our calculated spectrum enables us to assign the relatively intense transition around 10200 cm^{-1} to the spin-forbidden transition $^5A_1(D) \rightarrow {}^3E(H)$. We also observe the contribution of several spin-forbidden transitions around 20000 cm^{-1}, which might explain the width of this broad feature. The mixing parameters used in the present case give a very small number of $4p$ electrons $\langle N_{4p} \rangle = 8.7 \times 10^{-4}$.

The XAS spectrum in Fig. 2(f) presents two small features separated by 1 eV and a maximum intensity similar to the octahedral case (~2% of the edge jump and pre-edge area $A_{exp} = 5.6 \times 10^{-2}$ eV). For the calculations, we used a broadening of FWHM = 0.35 eV and the same hybridization values as in the ground state, the crystal-field values in both electron configurations are the ones given in Schofield *et al.* [52]. It can be noted that the crystal-field parameters used for the initial and final states of XAS slightly differ because it was not possible to reproduce both XAS and OAS spectra with a common set of parameters. Nonetheless, the ground-state term remains unchanged for both sets of parameters.

The calculation of the pre-edge feature using C_{4v} symmetry enables to reproduce the experimental features and reveals the multiplet states that compose this K pre-edge. The hybridization was set to the same values as the optical spectrum calculation. The total area, $A_{sum} = 6.9 \times 10^{-2}$ eV, is higher than the experimental one due to the tails of the spectrum that decrease faster in the experimental spectrum. The resulting dipole contribution arising from p-d mixing is not the reason of this area difference, and E1 explains only 1.8% of the total pre-edge area, which is similar to the dipole contribution estimated in the octahedral case. This corresponds to a very small number of $4p$ electrons in the final state ($\langle N_{4p} \rangle = 6.1 \times 10^{-4}$). The small E1 contribution and the small number of $4p$ electrons for both ground and excited states confirm that the local geometry of Fe^{2+} in gillespite remains close to the centrosymmetric D_{4h} site.

D. $^{[5]}Fe^{2+}$ in trigonal bipyramidal geometry

Grandidierite is a silicate mineral in which Fe^{2+} is fivefold coordinated in a distorted trigonal bipyramidal site with C_s symmetry. Experimental and calculated OAS spectra are presented in Fig. 2(g). The experimental optical spectrum of Fe^{2+} in grandidierite exhibits transitions occurring around 5000 cm^{-1} and in the range 10000–15000 cm^{-1}, attributed to two spin-allowed transitions $^5E(E_g) \rightarrow {}^5E(T_{2g})$ and $^5E(E_g) \rightarrow {}^5A_1$, respectively. However, the band centered at 12000 cm^{-1} is very broad (FWHM = 6500 cm^{-1}). Such a large width cannot be assigned to the crystal-field splitting of the $^5A_1$ term in lower symmetry, nor to the spin-orbit coupling, which only splits the levels by 800 cm^{-1}. This broad band seems to be composed of at least two contributions at 10200 and 13100 cm^{-1}, respectively. In order to explain such a splitting, Rossman and Taran [31] suggested the presence of several nonequivalent $^{[5]}Fe^{2+}$ sites in the grandidierite mineral. As a consequence, we included this hypothesis in our calculations by considering two sites named A and B. As seen above for sixfold coordinated Fe^{2+} in siderite, the crystal field of C_{3v} symmetry can be described by three parameters Dq, $D\sigma$, and $D\tau$ [37]. In the case of grandidierite, optical calculations were done with $\beta = 0.59$ and a Gaussian broadening of FWHM = 0.18 eV (1450 cm^{-1}). With the crystal-field and mixing parameters listed in Table II, the ground state is the $^5E(E_g)$ term for both sites (see Fig. 5).

The two optical spectra calculated for sites A and B of Fe^{2+} in C_{3v} [Fig. 2(g)] differ mainly by the value of $D\sigma$ and $D\tau$.

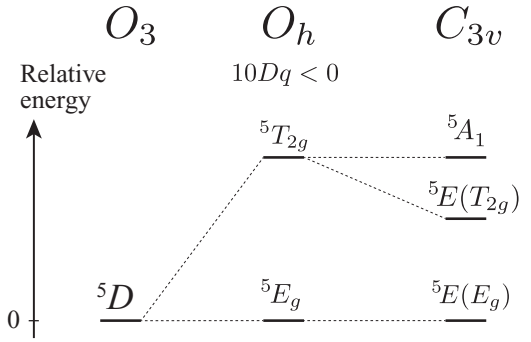

FIG. 5. Lifting of degeneracy of the ^5D spectroscopic term (free Fe^{2+} ion) caused by tetragonal distortion in the case of grandidierite.

They both show the two spin-allowed transitions with the first band, attributed to ${}^5E(E_g) \rightarrow {}^5E(T_{2g})$, around 5000 cm^{-1} for both sites. The second band, attributed to ${}^5E(E_g) \rightarrow {}^5A_1$, is present around 10000 cm^{-1} and 13000 cm^{-1} for sites A and B, respectively.

C_{3v} was chosen instead of D_{3h} symmetry, characteristic of regular trigonal bipyramidal for fivefold coordinated ions because the transition ${}^5E'' \rightarrow {}^5A'_1$ in the range 10000–15000 cm^{-1} is symmetry-forbidden in D_{3h} group [53]. We have shown here, that the approximation of the C_s point group to the C_{3v} point group was sufficient to accurately reproduce the experimental relative intensities and positions. Therefore the use of a lower point group, closer to the real grandidierite sites (as C_s or C_{2v}) is not necessary to fit experimental data, and could lead to overparametrized calculations. In other words, OAS are not sensitive to symmetries lower than C_{3v} in that case.

The experimental Fe K pre-edge spectrum [Fig. 2(h)] shows two main features at 7112.4 and 7114.1 eV separated by 1.7 eV. The maximum intensity is approximately equal to 5% of the edge jump, which is intermediate between O_h and T_d cases. The calculated spectrum was obtained by reducing the crystal-field parameters of the final state using 90% of the values used for optical calculations. The same hybridization values were used for all electronic states (Table II). XAS spectra were broadened with a Gaussian function with FWHM = 0.42 eV. The total intensity of the experimental pre-edge ($A_{exp} = 11.8 \times 10^{-2}$ eV) is similar to the calculation ($A_{sum} = 11.2 \times 10^{-2}$ eV). For both sites (A and B), the electric dipole contribution corresponds to 50% of the total area of the pre-edge with $A_{dip} = 5.6 \times 10^{-2}$ eV. The contribution of the quadrupole transitions is only half of the total area of the pre-edge, which demonstrates the necessity to account for $3d$-$4p$ hybridization. XAS calculations reveal that sites A and B lead to similar spectra, and only one of the two sites is sufficient to fully reproduce XAS experimental data and to attribute the transitions using C_{3v} point group. On the other hand, OAS calculation demonstrated the necessity to consider two crystallographic sites in the interpretation of the absorption spectrum.

V. DISCUSSION

A. Choice of the point group symmetry of the calculation

As described in the introduction, the absence of an inversion center is a *sine qua non* condition to allow the mixing of d states with p states and the calculation of nonzero electric dipole d-d-like optical transitions.

In the two cases of siderite ($^{[6]}Fe^{2+}$ in C_{3i}) and gillespite ($^{[4]}Fe^{2+}$ in C_{4v}), Fe ions occupy "almost" centrosymmetric sites. The experimental observation of optical absorption in both cases proves that the inversion center has been removed either by: a static distortion in gillespite, with the Fe ion 0.06 Å out of the square plane, giving C_{4v} point group; a dynamic breaking of the inversion center in siderite that we described by using C_{3v} point group instead of C_{3i}. The choice of these two point groups for our calculations enables the accurate description of the energy splittings of the $3d$ states with distortion and the observed transition intensities.

In the two noncentrosymmetric cases studied in this work: staurolite ($^{[4]}Fe^{2+}$ in C_{2v}) and grandidierite ($^{[5]}Fe^{2+}$ in C_s), the exact point groups of the Fe site are low, which would have lead to an unreasonably high number of crystal-field and hybridization parameters. The crystal-field Hamiltonian is a combination of terms with $k = 0$, 2, or 4 [Eq. (3)], and thus can contain up to 15 terms, while the hybridization Hamiltonian ($k = 1$ and 3) can contain up to ten parameters. Our calculations show that the approximation of the real point group to a higher point group symmetry fairly enables us to reproduce the optical and K pre-edge structures in the cases of staurolite and grandidierite.

This reveals that the choice of the point group symmetry used for the calculation is crucial. A general advice would be to first choose the largest possible noncentrosymmetric point group compatible with the approximate geometry of the site; then depending on the necessity to render for energy splittings (such as the splitting of the ground state in C_{3v} for siderite) or for transitions. The latter effect is well accounted for by the case of grandidierite. The appropriate choice of the point group provides in this case a deep insight into the origin of the optical transitions. Although the exact point group of Fe is C_s, the bipyramidal geometry could have been approximated by D_{3h} symmetry. However, as shown by our calculations, the transition to the ${}^5A_1$ (C_{3v}) state becomes allowed thanks to the mixing with p states when removing the horizontal symmetry plane of the D_{3h} point group.

B. Crystal-field and hybridization parameters

The hybridization Hamiltonian affects the energy position of the d states. The larger the hybridization parameter, the stronger this effect. An energy shift of the energy level diagram of Fe^{2+} ground state is induced by the hybridization Hamiltonian when using a non zero value of V_{pd}. As an example, in T_d symmetry, this is due to the mixing of the d orbitals of t_2 symmetry with the p orbitals of t_2 symmetry, which produces a symmetric combination of lower energy. To compensate for this energy shift in the calculated spectra, the $10Dq$ parameter has thus been increased. Compared with the results for staurolite in Arrio *et al.* [11], the present $10Dq$ value has been doubled to keep the OAS spin-allowed transition around 5000 cm^{-1}. This proves how important is the calculation of the optical absorption spectrum in order to define the ground state and illustrates the complementarity of OAS and XAS methods to determine the spectroscopic behavior of transition metals.

However, in the calculation of the K pre-edge, the nature of the ground state (at 300 K) prevails over the exact determination of all initial state energy levels. The shape of the K pre-edge is dominated by the energy splittings of the final state and the selection rules. In the calculation of XAS, the parameters of the final configuration is often taken to be different from those of the initial one to account for the electronic relaxation around the $1s$ core hole [3]. In our calculations, we only applied a reduction by 90% for the parameters of the final state of grandidierite, the parameters for gillespite were also modified, but not for siderite and staurolite. As long as the ground state remains identical, the K pre-edge spectrum only depends on the final state parameters. In all

TABLE III. Number of $4p$ electrons in the ground state and fraction of the pre-edge area coming from E1 transitions.

Sample	CN	Site symmetry	$\langle N_{4p} \rangle$	%E1
Siderite	6	C_{3v}	0.0027	5
Staurolite	4	T_d	0.1171	80
Gillespite	4	C_{4v}	0.0006	2
Grandidierite (A)	5	C_{3v}	0.0349	50
Grandidierite (B)	5	C_{3v}	0.0354	50

cases, our calculations prove the complex multiplet structure underlying the broad K pre-edge features. The attribution of the transitions using the d^{N+1} approximation confirms the weak effect of the $1s$ core hole as compared to the effect of the $2p$ core hole in L edges [54].

The simultaneous calculations of both optical and K pre-edge features enable us to constrain the fitting of the parameters of the ground state and XAS final state and prove that a multispectroscopic approach is important, if not crucial, to correctly describe the studied compound.

C. Point group symmetry and intensities

The contribution of the electric dipole transitions arises from the presence of a small amount of $4p$ states in the ground state. This is explicitly shown by the calculation of the number of $4p$ electrons as given in Table III. The number of $4p$ electrons in the ground state is correlated with the percentage of the dipole contribution in the K pre-edge. We observe that for almost centrosymmetric sites, a very small amount of $4p$ electrons is enough to bring out the optical transitions, whereas the K pre-edge mainly originates from electric quadrupole transitions. When p-d mixing is negligible, the contribution from the electric quadrupole transitions gives the same integrated peak area for both siderite and gillespite, in agreement with the sum rules. This confirms that optical transitions arise from symmetry breaking of the parity selection rule that forbids electric dipole transitions and that p-d mixing is the main origin of optical transitions.

For noncentrosymmetric sites the fraction of electric dipole transitions contributing to the K pre-edge intensity varies from 50% (grandidierite) to 80% (staurolite), which corresponds to an increase by 60%. However, as in Table III, the number of $4p$ electrons has more than tripled between both calculations. On the contrary, from grandidierite to siderite, which we both describe with C_{3v} point group, the fraction of dipole contribution decreases by a factor of 10, and the number of $4p$ electrons decreases by a factor of 13, suggesting a rather proportional relation between the electric dipole contribution and the number of $4p$ electrons. This reveals that two distinct effects control the amount of electric dipole contribution: (i) the fraction of p states that are mixed and (ii) the point group symmetry itself and the intrinsic selection rules that it carries.

VI. CONCLUSION

The semiempirical approach based on crystal-field theory and used in this work, has enabled us to reproduce both experimental optical and K pre-edge x-ray absorption spectra with a fair accuracy and a reasonable number of parameters. The present calculations were successful for reproducing both optical and K pre-edge x-ray absorption spectra for four distinct site symmetries found in minerals, i.e., a distorted octahedron (siderite), a distorted tetrahedron (staurolite), a square planar site (gillespite), and a trigonal bipyramidal site (grandidierite). The originality of this work resides in the combined calculations of OAS and XAS by using a single set of ground state parameters to reproduce the experimental features. The difference of sensitivity of OAS and XAS to the crystal-field and hybridization parameters is clearly pointed out, and more specifically the sensitivity of OAS to 10Dq. We were also able to quantify the influence of the symmetry on the fraction of $4p$ states in the ground state as a function of the point group symmetry of the absorbing site. The good agreement obtained between calculations and experiment demonstrates the validity of the approximations made in this model and the pertinence of using the ligand field multiplet calculations to extract information from experimental spectra.

Progress in the interpretation of the absorption spectra of TM and in particular of the intensity of the spectra offers powerful tools for determining the speciation of TM in complex materials such as impurities in crystals, oxide glasses, or reaction site on surfaces in inorganic chemistry and catalysis. In these cases, conventional diffraction techniques may not succeed in determining the exact site geometry but the combination of optical absorption and x-ray absorption (in particular K pre-edge features) spectroscopies is a key alternative method for probing the $3d$ levels of transition metal ions. XAS is particularly needed for d^0 compounds or nontransparent compounds. Full understanding of the experimental results relies on our ability to compute optical and x-ray spectra accounting for multielectronic interactions in order to derive information on the ground state.

ACKNOWLEDGMENTS

This work was supported by ANRT (CIFRE Contract 2012/0640), by AGC, by the Centre National de la Recherche Scientifique (CNRS, France), and the Ministère de l'Enseignement Supérieur et de la Recherche (MESR, France). The authors would like to thank AGC for their support. We acknowledge Jean-Claude Boulliard (IMPMC, University Pierre and Marie Curie, France) and François Farges (IMPMC, Museum National d'Histoire Naturelle, France) for providing the four minerals under study, Stéphanie Rossano (LGE, Université Paris-Est Marne-la-Vallée) for fruitful discussion on optical spectroscopy, George Rossman (California Institute of Technology, Pasadena, California, USA) for the use of grandidierite optical absorption data, Maxime Guillaumet (IMPMC, University Pierre and Marie Curie, France) for his help in optical data acquisition and Pieter Glatzel, Mauro Rovezzi, and Lucia Amidani (ESRF) for their help in Fe K pre-edge XAS data acquisition and for helpful discussions.

APPENDIX A: EXPRESSION OF CRYSTAL-FIELD AND HYBRIDIZATION HAMILTONIAN IN SECOND QUANTIZATION

We can write the crystal-field and hybridization Hamiltonians in second quantization as

$$H_{\mathrm{CF/Hyb}} = \sum_{\tau_1,\tau_2} \langle \varphi_{\tau_1}(\vec{r})|V(\vec{r})|\varphi_{\tau_2}(\vec{r})\rangle a^{\dagger}_{\tau_1} a_{\tau_2}, \tag{A1}$$

where $\varphi_\tau(\vec{r}) = R_{n\ell}(r)Y_{\ell,m}(\theta,\phi)$ is the local atomic orbitals indexed by the quantum number τ standing for the combination of n (principal quantum number), ℓ (orbital angular momentum), and m (magnetic quantum number). In order to evaluate $\langle \varphi_{\tau_1}(\vec{r})|V(\vec{r})|\varphi_{\tau_2}(\vec{r})\rangle$, we expand $V(\vec{r})$ over normalized spherical harmonics (Ref. [33], p. 146) defined by

$$C_{k,m}(\theta,\phi) = \sqrt{\frac{4\pi}{2k+1}} Y_{k,m}(\theta,\phi) \tag{A2}$$

and we obtain [34,37–39]

$$V(r,\theta,\phi) = \sum_{k,m} V_{k,m}(r) C_{k,m}(\theta,\phi), \tag{A3}$$

therefore

$$\langle \varphi_{\tau_1}|V|\varphi_{\tau_2}\rangle = \sum_{k,m} A_{k,m} \langle Y_{l_1,m_1}|C_{k,m}|Y_{l_2,m_2}\rangle, \tag{A4}$$

with

$$A_{k,m} = \int R^*_{n_1\ell_1}(r) V_{k,m}(r) R_{n_2\ell_2} r^2 dr, \tag{A5}$$

where

$$V_{k,m}(r) = \sqrt{\frac{2k+1}{4\pi}} \int V(\vec{r}) Y^*_{k,m}(\theta,\phi) \sin(\theta) d\theta d\phi. \tag{A6}$$

APPENDIX B: RELATIONS BETWEEN PARAMETERS AND $A_{k,m}$, ENERGIES

For a $3d$ transition metal, the crystal-field Hamiltonian is written as

$$H_{\mathrm{CF}} = \sum_{\substack{k=0,\\ k\ \mathrm{even}}}^{4} \sum_{m=-k}^{k} A_{k,m} C_{k,m}(\theta,\phi). \tag{B1}$$

In the following, we will also give the expression using the more common crystal-field parameters defined by König-Kremer [37].

For $3d$ transition metal, the p-d hybridization Hamiltonian is written as

$$H_{\mathrm{Hyb}} = \sum_{\substack{k=1,\\ k\ \mathrm{odd}}}^{3} \sum_{m=-k}^{k} A_{k,m} C_{k,m}(\theta,\phi). \tag{B2}$$

1. T_d symmetry

The tetrahedron is oriented with the three C_2 axes along x, y, and z axes, and the four C_3 axes along the diagonals of the cube (Fig. 6).

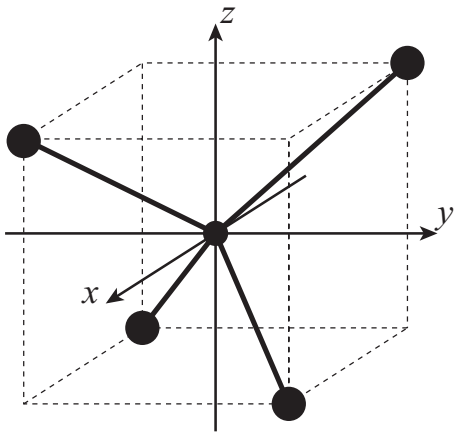

FIG. 6. Orientation of the tetrahedron.

The nonzero $A_{k,m}$ are obtained by using symmetry operations and the hermitian nature of the Hamiltonian giving $A_{k,m} = (-1)^m A^*_{k,-m}$ [38]. In T_d symmetry, the nonzero $A_{k,m}$ with $k \leqslant 4$ and $-4 \leqslant m \leqslant 4$ are: $A_{0,0}$ (real), $A_{3,2} = -A_{3,-2}$ (pure imaginary), and $A_{4,0} = \sqrt{\frac{14}{5}} A_{4,4} = \sqrt{\frac{14}{5}} A_{4,-4}$ (real).

a. Crystal-field Hamiltonian

In T_d symmetry, the crystal-field Hamiltonian is written as

$$\begin{aligned} H^{T_d}_{\mathrm{CF}} &= A_{4,0}C_{4,0} + \sqrt{\frac{5}{14}} A_{4,0}(C_{4,-4} + C_{4,4}) \\ &= 21DqC_{4,0} + 21\sqrt{\frac{5}{14}} Dq(C_{4,-4} + C_{4,4}). \end{aligned} \tag{B3}$$

In T_d group symmetry, the cubic d orbitals are separated in two groups: $d_{z^2}, d_{x^2-y^2}$ transform as the e irreducible representation and d_{xy}, d_{xz}, d_{yz} as the t_2 irreducible representation. The $A_{k,m}$ of the Hamiltonian H_{CF} are related to the energy of the d orbitals (without p-d hybridization) as

$$\begin{aligned} A_{0,0} &= \frac{3}{5}E^{t_2}_d + \frac{2}{5}E^{e}_d, \\ A_{4,0} &= \frac{21}{10}\left(E^{e}_d - E^{t_2}_d\right), \\ A_{4,4} = A_{4,-4} &= \frac{3}{2}\sqrt{\frac{7}{10}}\left(E^{e}_d - E^{t_2}_d\right). \end{aligned} \tag{B4}$$

The relationship between the energy of the cubic d orbitals and the crystal-field parameter Dq is (Ref. [37], p. 21, Eq. (3.86)):

$$\begin{aligned} E^{e}_d &= 6Dq, \ (d_{z^2}, d_{x^2-y^2}), \\ E^{t_2}_d &= -4Dq, \ (d_{xy}, d_{xz}, d_{yz}), \end{aligned} \tag{B5}$$

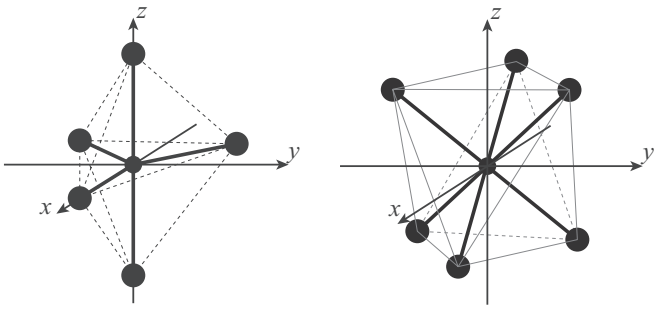

FIG. 7. Orientation of the trigonal bipyramid and the octahedron in C_{3v}.

after replacing in the previous equations, we get

$$\begin{aligned} A_{0,0} &= 0, \\ A_{4,0} &= 21Dq, \\ A_{4,4} &= A_{4,-4} = 21\sqrt{\frac{5}{14}}Dq. \end{aligned} \tag{B6}$$

In T_d, $10Dq < 0$ (i.e., $E_d^e < E_d^{t_2}$). The definition of the crystal-field Hamiltonian is identical for O_h symmetry, except that the notation e is changed to e_g, t_2 to t_{2g} and that $10Dq > 0$ (i.e., $E_d^{e_g} > E_d^{t_{2g}}$)

b. Hybridization Hamiltonian

In T_d symmetry that does not have a center of symmetry, the hybridization Hamiltonian is defined by

$$H_{\text{Hyb}}^{T_d} = i\frac{7}{\sqrt{6}}(C_{3,2} - C_{3,-2})V_{pd}^{t_2} \tag{B7}$$

with $V_{pd}^{t_2} = i\frac{\sqrt{6}}{7}A_{3,2}$. $V_{pd}^{t_2}$ is real since $A_{3,2}$ is a pure imaginary number. In this work, we used $V_{pd}^{t_2} = \frac{1}{\sqrt{21}}V_{pd}$, where V_{pd} is the value used in Arrio *et al.* [11].

c. Matrix in the cubic basis

In the cubic basis of p and d real orbitals the matrix of the total Hamiltonian $H_{\text{CF}} + H_{\text{Hyb}}$ is given by

	d_{xy}	d_{yz}	$d_{3z^2-r^2}$	d_{xz}	$d_{x^2-y^2}$	p_x	p_y	p_z
d_{xy}	$E_d^{t_2}$	0	0	0	0	0	0	$V_{pd}^{t_2}$
d_{yz}	–	$E_d^{t_2}$	0	0	0	$V_{pd}^{t_2}$	0	0
$d_{3z^2-r^2}$	–	–	E_d^e	0	0	0	0	0
d_{xz}	–	–	–	$E_d^{t_2}$	0	0	$V_{pd}^{t_2}$	0
$d_{x^2-y^2}$	–	–	–	–	E_d^e	0	0	0
p_x	–	–	–	–	–	$E_p^{t_2}$	0	0
p_y	–	–	–	–	–	–	$E_p^{t_2}$	0
p_z	–	–	–	–	–	–	–	$E_p^{t_2}$

2. C_{3v} symmetry in the basis of the irreducible representation

For C_{3v} symmetry, we chose the C_3 axis along the z axis, and one of the three C_2 axes along the x axis (Fig. 7). Instead of using the cubic d basis, one can use the C_{3v} irreducible representation of Butler group tables [34]. The d cubic orbitals (in the x, y, and z axes chosen for C_{3v}) transform as

$$\begin{aligned} e_+(e_g) &= \frac{d_{x^2-y^2}}{\sqrt{6}} + \frac{id_{xy}}{\sqrt{6}} + \frac{d_{xz}}{\sqrt{3}} - \frac{id_{yz}}{\sqrt{3}}, \\ e_-(e_g) &= \frac{d_{x^2-y^2}}{\sqrt{6}} - \frac{id_{xy}}{\sqrt{6}} + \frac{d_{xz}}{\sqrt{3}} + \frac{id_{yz}}{\sqrt{3}}, \\ a_1(t_{2g}) &= -d_{3z^2-r^2}, \\ e_+(t_{2g}) &= -\frac{d_{x^2-y^2}}{\sqrt{3}} - \frac{id_{xy}}{\sqrt{3}} + \frac{d_{xz}}{\sqrt{6}} - \frac{id_{yz}}{\sqrt{6}}, \\ e_+(t_{2g}) &= -\frac{d_{x^2-y^2}}{\sqrt{3}} + \frac{id_{xy}}{\sqrt{3}} + \frac{d_{xz}}{\sqrt{6}} + \frac{id_{yz}}{\sqrt{6}}. \end{aligned} \tag{B8}$$

Indicated in the parenthesis is the O_h irreducible representation from which the C_{3v} irreducible representation originates. In C_{3v} symmetry, the nonzero $A_{k,m}$ with $k \leqslant 4$ and $-4 \leqslant m \leqslant 4$ are: $A_{0,0}$ (real), $A_{1,0}$ (real), $A_{2,0}$ (real), $A_{3,0}$ (real), $A_{3,3} = -A_{3,-3}$ (real), $A_{4,0}$ (real), and $A_{4,3} = -A_{4,-3}$ (real).

a. Crystal-field Hamiltonian

In C_{3v} symmetry, the crystal-field Hamiltonian is written as

$$\begin{aligned} H_{\text{CF}}^{C_{3v}} &= A_{2,0}C_{2,0} + A_{4,0}C_{4,0} + A_{4,3}(C_{4,3} - C_{4,-3}) \\ &= -7D\sigma C_{2,0} - (14Dq + 21D\tau)C_{4,0} \\ &\quad + 2\sqrt{70}Dq(C_{4,-3} - C_{4,3}). \end{aligned}$$

The crystal-field matrix is not diagonal but the diagonal matrix elements are often close to the eigenenergies. One defines

$$\begin{aligned} E_d^{e(e_g)} &= \langle e_\pm(e_g)|H_{\text{CF}}|e_\pm(e_g)\rangle, \\ E_d^{a_1(t_{2g})} &= \langle a_1(t_{2g})|H_{\text{CF}}|a_1(t_{2g})\rangle, \\ E_d^{e(t_{2g})} &= \langle e_\pm(t_{2g})|H_{\text{CF}}|e_\pm(t_{2g})\rangle. \end{aligned} \tag{B9}$$

The relationship between the $A_{k,m}$ and the matrix elements is

$$\begin{aligned} E_d^{e(e_g)} &= -\frac{1}{9}A_{4,0} - \frac{2}{9}\sqrt{\frac{10}{7}}A_{4,3}, \\ E_d^{a_1(t_{2g})} &= \frac{2}{7}A_{2,0} + \frac{2}{7}A_{4,0}, \\ E_d^{e(t_{2g})} &= -\frac{1}{7}A_{2,0} - \frac{2}{63}A_{4,0} + \frac{2}{9}\sqrt{\frac{10}{7}}A_{4,3}, \\ \langle e_\pm(t_{2g})|H_{\text{CF}}|e_\pm(e_g)\rangle &= -\frac{\sqrt{2}}{7}A_{2,0} + \frac{5\sqrt{2}}{63}A_{4,0} - \frac{1}{9}\sqrt{\frac{5}{7}}A_{4,3}. \end{aligned} \tag{B10}$$

In the case of C_{3v} symmetry, it is not possible to express the $A_{k,m}$ in terms of the diagonal matrix elements because the rank of the augmented matrix associated to the system of linear equations is 2 and there are 3 non-zero parameters.

The relationship between the matrix elements and the crystal-field parameters defined by König-Kremer [37,40] is

$$\begin{aligned} E_d^{e(e_g)} &= 6D + \frac{7}{3}D\tau, \\ E_d^{a_1(t_{2g})} &= -4Dq - 2D\sigma - 6D\tau, \\ E_d^{e(t_{2g})} &= -4Dq + D\sigma + \frac{2}{3}D\tau, \\ \langle e_\pm(t_{2g})|H_{\text{CF}}|e_\pm(e_g)\rangle &= -\frac{\sqrt{2}}{3}(3D\sigma - 5D\tau), \end{aligned} \tag{B11}$$

after replacing in the previous equations, we get

$$\begin{aligned} A_{0,0} &= 0, \\ A_{2,0} &= -D\sigma, \\ A_{4,0} &= -14Dq - 21D\tau, \\ A_{4,3} &= -2\sqrt{70}Dq. \end{aligned} \tag{B12}$$

b. Hybridization Hamiltonian

The p cubic orbitals (in the x, y, and z axes chosen for C_{3v}) transform as

$$\begin{aligned} a_1(t_{1u}) &= p_z, \\ e_\pm(t_{1u}) &= \frac{1}{\sqrt{2}}(p_x \pm ip_y). \end{aligned} \tag{B13}$$

Indicated in parentheses is the O_h irreducible representation from which the C_{3v} irreducible representation originates.

In C_{3v} symmetry, p and d orbitals can mix along two irreducible representations: a_1 and e. Since the d orbitals transform as one a_1 and two e irreducible representations [$e(e_g)$ and $e(e_{t_{2g}})$], the hybridization Hamiltonian can be separated in three terms:

$$H_{\rm Hyb}^{C_{3v}} = H_{\rm Hyb}^{e(e_g)} + H_{\rm Hyb}^{a_1(t_{2g})} + H_{\rm Hyb}^{e(t_{2g})},$$

where

$$H_{\rm Hyb}^{a_1(t_{2g})} = \left(-\sqrt{\frac{3}{5}}C_{1,0} - \frac{7}{\sqrt{15}}C_{3,0}\right)V_{pd}^{a_1(t_{2g})},$$

$$H_{\rm Hyb}^{e(e_g)} = \left(\sqrt{\frac{6}{5}}C_{1,0} - \frac{14}{3}\sqrt{\frac{2}{15}}C_{3,0} - \frac{7}{3\sqrt{3}}(C_{3,3} - C_{3,-3})\right) \times V_{pd}^{e(e_g)},$$

$$H_{\rm Hyb}^{e(t_{2g})} = \left(\sqrt{\frac{3}{5}}C_{1,0} - \frac{14}{3\sqrt{15}}C_{3,0} + \frac{7}{3}\sqrt{\frac{2}{3}}(C_{3,3} - C_{3,-3})\right) \times V_{pd}^{e(t_{2g})}, \tag{B14}$$

where the V_{pd} hybridization coefficients are related to the $A_{k,m}$ by

$$\begin{aligned} V_{pd}^{a_1(t_{2g})} &= -\frac{2}{\sqrt{15}}A_{1,0} - \frac{3}{7}\sqrt{\frac{3}{5}}A_{3,0}, \\ V_{pd}^{e(e_g)} &= \sqrt{\frac{2}{15}}A_{1,0} - \frac{1}{7}\sqrt{\frac{6}{5}}A_{3,0} - \frac{1}{7}\sqrt{3}A_{3,3}, \\ V_{pd}^{e(t_{2g})} &= \frac{1}{\sqrt{15}}A_{1,0} - \frac{1}{7}\sqrt{\frac{3}{5}}A_{3,0} + \frac{1}{7}\sqrt{6}A_{3,3}. \end{aligned} \tag{B15}$$

c. Matrix

In the basis of the C_{3v} irreducible representations, the matrix of the total Hamiltonian $H_{\rm CF} + H_{\rm Hyb}$ is

	d $e_+(e_g)$	d $e_-(e_g)$	d $a_1(t_{2g})$	d $e_+(t_{2g})$	d $e_+(t_{2g})$	p $a_1(t_{1u})$	p $e_+(t_{1u})$	p $e_-(t_{1u})$
$e_+(e_g)$	$E_d^{e(e_g)}$	0	0	$\frac{5}{3}\sqrt{2}D\tau - \sqrt{2}D\sigma$	0	0	$V_{pd}^{e(e_g)}$	0
$e_-(e_g)$	–	$E_d^{e(e_g)}$	0	0	$\frac{5}{3}\sqrt{2}D\tau - \sqrt{2}D\sigma$	0	0	$V_{pd}^{e(e_g)}$
$a_1(t_{2g})$	–	–	$E_d^{a_1(t_{2g})}$	0	0	$V_{pd}^{a_1(t_{2g})}$	0	0
$e_+(t_{2g})$	–	–	–	$E_d^{e(t_{2g})}$	0	0	$V_{pd}^{e(t_{2g})}$	0
$e_+(t_{2g})$	–	–	–	–	$E_d^{e(t_{2g})}$	0	0	$V_{pd}^{e(t_{2g})}$
$a_1(t_{1u})$	–	–	–	–	–	$E_p^{e(t_{1u})}$	0	0
$e_+(t_{1u})$	–	–	–	–	–	–	$E_p^{e(t_{1u})}$	0
$e_-(t_{1u})$	–	–	–	–	–	–	–	$E_p^{e(t_{1u})}$

3. C_{4v} symmetry

In C_{4v}, the C_4 axis along the z-axis, and the x- and y-axes are normal to the σ_v planes (Fig. 8).

In C_{4v} symmetry, the nonzero $A_{k,m}$ with $k \leqslant 4$ and $-4 \leqslant m \leqslant 4$ are: $A_{0,0}$ (real), $A_{1,0}$ (real), $A_{2,0}$ (real), $A_{3,0}$ (real), $A_{4,0}$ (real), and $A_{4,4} = A_{4,-4}$ (real).

a. Crystal-field Hamiltonian

In C_{4v} symmetry, the cubic d orbitals are eigenfunctions of the crystal-field Hamiltonian. The $A_{k,m}$ of the Hamiltonian $V_{\rm CF}$ are related to the energy of the monoelectronic d levels as

$$\begin{aligned} A_{0,0} &= \tfrac{1}{5}\left(E_d^{a_1} + E_d^{b_1} + E_d^{b_2} + 2E_d^{e}\right), \\ A_{2,0} &= E_d^{a_1} - E_d^{b_1} - E_d^{b_2} + E_d^{e}, \\ A_{4,0} &= \tfrac{3}{10}\left(6E_d^{a_1} + E_d^{b_1} + E_d^{b_2} - 8E_d^{e}\right), \\ A_{4,4} &= A_{4,-4} = \tfrac{3}{20}\left(\sqrt{70}E_d^{b_1} - \sqrt{70}E_d^{b_2}\right). \end{aligned} \tag{B16}$$

The relationship between the energy of the real orbitals and the crystal-field parameters is (Ref. [37], p. 21, Eq. (3.84))

$$\begin{aligned} E_d^{a_1} &= 6Dq - 2Ds - 6Dt, (d_{z^2}), \\ E_d^{b_1} &= 6Dq + 2Ds - 1Dt, (d_{x^2-y^2}), \\ E_d^{b_2} &= -4Dq + 2Ds - 1Dt, (d_{xy}), \\ E_d^{e} &= -4Dq - 1Ds + 4Dt, (d_{xz}, d_{yz}). \end{aligned} \tag{B17}$$

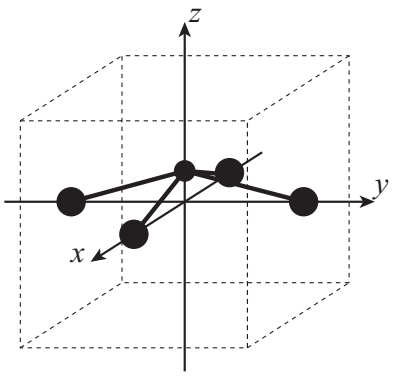

FIG. 8. Orientation for the C_{4v} geometry.

b. Hybridization Hamiltonian

In C_{4v} symmetry, p and d orbitals can mix along two irreducible representations: a_1 and e. Thus the hybridization Hamiltonian is defined by $H_{\rm Hyb}^{C_{4v}} = H_{pd}^{a_1} + H_{pd}^{e}$ with

$$\begin{aligned} H_{\rm Hyb}^{a_1(t_{2g})} &= \left(\sqrt{\frac{3}{5}}C_{1,0} + \frac{7}{\sqrt{15}}C_{3,0}\right)V_{pd}^{a_1(t_{2g})}, \\ H_{\rm Hyb}^{e(e_g)} &= \left(\frac{3}{\sqrt{5}}C_{1,0} - \frac{14}{3\sqrt{5}}C_{3,0}\right)V_{pd}^{e(e_g)}, \end{aligned} \tag{B18}$$

where

$$\begin{aligned} V_{pd}^{a_1} &= \frac{2}{\sqrt{15}}A_{1,0} + \frac{3}{7}\sqrt{\frac{3}{5}}A_{3,0}, \\ V_{pd}^{e} &= \frac{1}{\sqrt{5}}A_{1,0} - \frac{3}{7\sqrt{5}}A_{3,0}. \end{aligned} \tag{B19}$$

c. Matrix in the C_{4v} (cubic) basis

In the cubic basis of p and d orbitals, the matrix of the total Hamiltonian $H_{\rm CF} + H_{\rm Hyb}$ is given by

	d_{xy}	d_{yz}	$d_{3z^2-r^2}$	d_{xz}	$d_{x^2-y^2}$	p_x	p_y	p_z
d_{xy}	$E_d^{b_2}$	0	0	0	0	V_{pd}^{e}	0	0
d_{yz}	–	E_d^{e}	0	0	0	0	V_{pd}^{e}	0
$d_{3z^2-r^2}$	–	–	$E_d^{a_1}$	0	0	0	0	$V_{pd}^{a_1}$
d_{xz}	–	–	–	E_d^{e}	0	0	0	0
$d_{x^2-y^2}$	–	–	–	–	$E_d^{b_1}$	0	0	0
p_x	–	–	–	–	–	E_p^{e}	0	0
p_y	–	–	–	–	–	–	E_p^{e}	0
p_z	–	–	–	–	–	–	–	$E_p^{a_1}$

[1] I. B. Bersuker and V. Z. Polinger, *Vibrational Interactions in molecules and Crystals* (Springer-Verlag, Berlin, Heidelberg, 1989).
[2] M. O. J. Y. Hunault, L. Galoisy, G. Lelong, M. Newville, and G. Calas, J. Non-Cryst. Solids **451**, 101 (2016).
[3] T. E. Westre, P. Kennepohl, J. G. DeWitt, B. Hedman, K. O. Hodgson, and E. I. Solomon, J. Am. Chem. Soc. **119**, 6297 (1997).
[4] M. Hunault, J.-L. Robert, M. Newville, L. Galoisy, and G. Calas, Spectrochim. Acta A **117**, 406 (2014).
[5] M. Wilke, G. M. Partzsch, R. Bernhardt, and D. Lattard, Chem. Geol. **220**, 143 (2005).
[6] F. Farges, Phys. Chem. Miner. **36**, 463 (2009).
[7] T. Yamamoto, X-Ray Spectrom. **37**, 572 (2008).
[8] M. Wilke, F. Farges, P.-E. Petit, G. E. Brown, and F. Martin, Am. Mineral. **86**, 714 (2001).
[9] M. Wilke, F. Farges, G. M. Partzsch, C. Schmidt, and H. Behrens, Am. Mineral. **92**, 44 (2007).
[10] G. Calas, L. Cormier, L. Galoisy, and P. Jollivet, C.R. Chim. **5**, 831 (2002).
[11] M.-A. Arrio, S. Rossano, C. Brouder, L. Galoisy, and G. Calas, Europhys. Lett. **51**, 454 (2000).
[12] M. Hunault, V. Vercamer, M. W. Haverkort, M.-A. Arrio, C. Brouder, G. Calas, and A. Juhin, J. Phys.: Conf. Ser. **712**, 012005 (2016).
[13] S. Rossano, C. Brouder, M. Alouani, and M. A. Arrio, Phys. Chem. Miner. **27**, 170 (2000).
[14] C. J. Ballhausen and A. D. Liehr, J. Mol. Spectrosc. **2**, 342 (1958).
[15] A. J. Bridgeman and M. Gerloch, Coord. Chem. Rev. **165**, 315 (1997).
[16] A. D. Liehr and C. J. Ballhausen, Phys. Rev. **106**, 1161 (1957).
[17] K. Ogasawara, T. Ishii, I. Tanaka, and H. Adachi, Phys. Rev. B **61**, 143 (2000).
[18] T. Ishii, K. Fujimura, K. Ogasawara, H. Adachi, and I. Tanaka, J. Phys. Condens. Matter **13**, 5757 (2001).
[19] K. Saito, Y. Eishiro, Y. Nakao, H. Sato, and S. Sakaki, Inorg. Chem. **51**, 2785 (2012).
[20] S. Watanabe, T. Sasaki, R. Taniguchi, T. Ishii, and K. Ogasawara, Phys. Rev. B **79**, 075109 (2009).
[21] M. Novita and K. Ogasawara, Jpn J. Appl. Phys. **51**, 022604 (2012).
[22] V. Vercamer, G. Lelong, H. Hijiya, Y. Kondo, L. Galoisy, and G. Calas, J. Non-Cryst. Solids **428**, 138 (2015).
[23] C. W. White and N. H. Tolk, Phys. Rev. Lett. **26**, 486 (1971).
[24] H. Effenberger, K. Mereiter, and J. Zemann, Z. Kristallogr **156**, 233 (1981).
[25] V. Badaut, P. Zeller, B. Dorado, and M. L. Schlegel, Phys. Rev. B **82**, 205121 (2010).
[26] R. Oberti, F. C. Hawthorne, A. Zanetti, L. Ottolini, and J. I. Soto, Can. Mineral. **34**, 1051 (1996).
[27] R. M. Hazen and L. W. Finger, Am. Mineral. **68**, 595 (1983).
[28] D. A. Stephenson and P. B. Moore, Acta Crystallogr. Sect. B **24**, 1518 (1968).
[29] B. Ravel and M. Newville, J. Synchrotron Radiat. **12**, 537 (2005).
[30] B. Hapke, *Theory of Reflectance and Emittance Spectroscopy*, 2nd ed. (Cambridge University Press, Cambridge, 2012).
[31] G. R. Rossman and M. N. Taran, Am. Mineral. **86**, 896 (2001).
[32] B. T. Thole, R. D. Cowan, G. A. Sawatzky, J. Fink, and J. C. Fuggle, Phys. Rev. B **31**, 6856 (1985).

[33] R. D. Cowan, *The Theory of Atomic Structure and Spectra* (University of California Press, Berkeley, 1981).
[34] P. H. Butler, *Point Group Symmetry Applications: Methods and Tables* (Plenum Press, New-York, 1981).
[35] F. M. F. de Groot and A. Kotani, *Core Level Spectroscopy of Solids* (CRC Press, Boca Raton, 2008).
[36] M. Hunault, Ph.D. thesis, Université Pierre et Marie Curie, 2014, http://www.theses.fr/2014PA066315.
[37] E. König and S. Kremer, *Ligand Field Energy Diagrams* (Plenum Press, New-York, 1977).
[38] M. W. Haverkort, Ph.D. thesis, University of Cologne, 2005, arXiv:cond-mat/0505214v1.
[39] M. W. Haverkort, J. Phys. Conf. Ser. **712**, 012001 (2016).
[40] A. Juhin, C. Brouder, M.-A. Arrio, D. Cabaret, P. Sainctavit, E. Balan, A. Bordage, A. P. Seitsonen, G. Calas, S. G. Eeckhout *et al.*, Phys. Rev. B **78**, 195103 (2008).
[41] M. Taillefumier, D. Cabaret, A.-M. Flank, and F. Mauri, Phys. Rev. B **66**, 195107 (2002).
[42] E. M. Gullikson, X-ray Interactions with Matter, CXRO (2010), http://henke.lbl.gov/optical_constants/.
[43] A. B. P. Lever, *Inorganic Electronic Spectroscopy* (Elsevier, Amsterdam, 1984).
[44] R. G. Burns, *Mineralogical Applications of Crystal Field Theory* (Cambridge University Press, Cambridge, 1993).
[45] Z. Min-Guang and D. Mao-Lu, Phys. Rev. B **28**, 6481 (1983).
[46] Z. Yi-Yang and Y. Chun-Hao, Phys. Rev. B **47**, 5451 (1993).
[47] G. Calas and J. Petiau, Solid State Commun. **48**, 625 (1983).
[48] L. Galoisy, G. Calas, and M. A. Arrio, Chem. Geol. **174**, 307 (2001).
[49] C. J. Ballhausen, *Introduction to Ligand Field Theory* (McGraw-Hill, New-York, 1962).
[50] R. G. Burns, M. G. Clark, and A. J. Stone, Inorg. Chem. **5**, 1268 (1966).
[51] D. J. Mackey, R. F. McMeeking, and M. A. Hitchman, J. Chem. Soc. Dalton 299 (1979).
[52] P. F. Schofield, G. Van Der Laan, C. M. B. Henderson, and G. Cressey, Mineral. Mag. **62**, 65 (1998).
[53] W. E. Jackson, F. Farges, M. Yeager, P. A. Mabrouk, S. Rossano, G. A. Waychunas, E. I. Solomon, and G. E. Brown, Jr., Geochim. Cosmochim. Ac. **69**, 4315 (2005).
[54] F. M. F. de Groot, J. C. Fuggle, B. T. Thole, and G. A. Sawatzky, Phys. Rev. B **42**, 5459 (1990).